A software-assisted crystallographic approach for achieving specific beam orientations for transmission electron microscopy characterization

Luda Wang [a, b], Benoit Beausir [a], Yudong Zhang [a*], Claude Esling [a], Xiang Zhao [b], Hai-Le Yan [b*], Liang Zuo [b]*

[a] **Université de Lorraine, CNRS, LEM3, Metz, France**

[b] **Key Laboratory for Anisotropy and Texture of Materials, Ministry of Education, Northeastern University, Shenyang 110819, China**

*** Corresponding authors: benoit.beausir@univ-lorraine.fr, yudong.zhang@univ-lorraine.fr, yanhaile@mail.neu.edu.cn**

KEYWORDS
TEM
Diffraction contrast/phase contrast
Two-beam condition
Zone-axis on-edge
Crystallographic orientation
Stereographic projection

REFERENCE
A software-assisted crystallographic approach for achieving specific beam orientations for transmission electron microscopy characterization,
L. Wang, B. Beausir, Y. Zhang, C. Esling, X. Zhao, H.-L. Yan, L. Zuo, Journal of Applied Crystallography 2026, 59, 1.
https://doi.org/10.1107/S1600576725010118

ABSTRACT
TEM imaging relies on specific orientations of the incident electron beam relative to the sample in both conventional TEM and high-resolution TEM/STEM. In conventional TEM, contrast arises from diffraction, where elastically scattered electrons form diffracted beams at angles defined by the Bragg law. In high-resolution TEM/STEM, contrast results from phase interference between the transmitted and diffracted waves, each acquiring a distinct phase at the exit surface due to different path lengths. This interference can be constructive, destructive, or intermediate. The visibility of these contrasts depends critically on sample orientation. Traditionally, achieving optimal alignment has relied on empirical trial-and-error, requiring user expertise and considerable time. To overcome this limitation, we worked out a new method supported by a dedicatedly developed module in ATEX-software. This method leverages the determined crystal orientation, expressed by Euler angles with respect to the sample holder. It establishes the geometric relations between the incident beam, the desired diffraction vector g (for two-beam conditions) or a zone-axis (for on-axis imaging) and the tilt/rotation axes of the holder. Using this information, the software provides precise tilt and rotation instructions to reach the desired beam condition efficiently. Unlike conventional methods, this approach significantly reduces the alignment effort, typically requiring no more than two tilts of the sample holder.

1. Introduction

Transmission Electron Microscopy (TEM) is a powerful technique for characterizing microstructures across scales ranging from the mesoscale to the atomic scale. It plays a crucial role in revealing the fundamental mechanisms underlying physical, chemical, and metallurgical processes in metallic alloys, ceramics, intermetallics, and semiconductors. In this context, TEM utilizes either diffraction contrast (conventional TEM) or phase contrast (high-resolution TEM or STEM) to visualize key features such as crystal defects (dislocations, stacking faults, grain boundaries), crystal structures, phase precipitates, their orientation relationships (ORs), and atomic arrangements. Two fundamental diffraction conditions are widely used in TEM operation. The first is the two-beam condition (including the weak-beam condition) primarily employed for defect analysis [1, 2]. The second is the zone-axis on-edge condition, used for phase transformations [3, 4], OR analysis [5, 6], and atomic-scale imaging [7, 8]. For the two-beam condition, the crystal is oriented so that only one diffracted beam is strongly excited alongside the transmitted beam [9]. This condition produces specific contrast, ideal for imaging defected or strained crystal regions. It is extensively used to determine dislocation Burgers vectors [10, 11], visualize strain fields [12], and map defect configurations [13, 14]. In contrast, the zone-axis condition aligns the crystal such that a low-indexed lattice direction (zone-axis) is parallel to the incident electron beam, generating characteristic zone-axis diffraction patterns. This orientation is critical for crystal structure determination, OR analysis and precipitate identification. It is widely applied in high-resolution TEM (HRTEM) and STEM [15, 16], particularly in high-angle annular dark-field STEM (HAADF STEM) imaging [17, 18].

Despite the powerful analytical capabilities of TEM, its exploratory potential is often challenged by the complex crystallographic nature of samples, diffraction dynamics and the constraints associated with sample mounting. Finding the appropriate beam or imaging condition becomes a routine yet critical aspect of TEM work, occupying a substantial portion of the experimental effort. Traditionally, achieving the desired beam conditions involves a trial-and-error approach, requiring iterative adjustments and the expertise of a skilled operator to manually control specimen tilt and rotation. This process is highly time-consuming and prone to misalignment, especially when dealing with materials exhibiting complex crystal structures.

To address these challenges, software- and computer-assisted protocols have been developed over the years to streamline specific aspects of TEM analysis. One notable advancement has been the implementation of computer-aided image matching techniques for dislocation Burgers vector determination. These methods rely on comparing experimental dislocation contrast with that of the simulated images [19-22], significantly facilitating the analysis. However, the actual acquisition of suitable TEM images still remains a matter of chance, depending heavily on operator intuition and manual exploration. More recently, the emergence of crystal orientation determination techniques [23-26] has enabled simulation-based guidance for tilting the sample to achieve specific beam conditions such as $\boldsymbol{g} \cdot \boldsymbol{b} = 0$, crucial for Burgers vector identification. These software-supported strategies have meaningfully simplified the experimental workflow. Yet, despite these advances, there remains a strong need for a general, systematic, and practical experimental

Permanent link http://www.atex-software.eu/papers/ATEX_TEM_Aligner_Paper.pdf
D O I https://doi.org/10.1107/S1600576725010118

approach that ensures reliable access to a wide range of beam orientation conditions essential for routine TEM analysis.

In this work, we elaborate a general and innovative software-assisted approach to directly achieve the required beam orientation conditions in TEM for various analytical purposes, including defect characterization, crystal structure determination, precipitate identification and orientation relationship (OR) analysis, based on crystallographic orientation data. The developed method is implemented as a dedicated module within the freeware – ***Analysis Tools for Electron and X-ray diffraction, ATEX-software*** [28]. By using systematic crystallographic calculations and orientation mapping (via pole figures), this approach enables precise and efficient control of sample rotation and tilt to reach the desired imaging conditions. This strategy not only streamlines the experimental workflow, reducing the need for time-consuming trial-and-error adjustments, but also significantly improves the accuracy and reproducibility of TEM-based analyses. Furthermore, it holds potential not only for routine users of TEM but also for instrument developers, offering a robust framework for integrating automated sample alignment and orientation control.

2. Methodology

2.1. Setting of coordinate systems and their orientation relationships

Considering the characteristics of TEM for sample loading and imaging, two Cartesian (orthonormal) coordinate systems are introduced in addition to the Cartesian crystal coordinate system (***i-j-k***) to the studied crystal (grain). One is set to the sample holder (***X_{sh}-Y_{sh}-Z_{sh}***) that has the ***Z_{sh}*** axis parallel to the incident beam and the ***X_{sh}*** axis parallel to the tilt axis of the sample holder and the other (***X_s-Y_s-Z_s***) to the TEM screen with its ***Z_s*** axis parallel to the incident beam. The relation between each pair of coordinate systems is defined by a triplet of rotations (Euler angles in Bunge notation [29]) that allows coordinate transformation from one to another [30], as shown in Fig. 1. The relation between the sample holder and the crystal coordinate system (represented by (φ_1, Φ, φ_2)) can be directly determined by indexing the obtained Kikuchi or the spot pattern, using the dedicated software packages [27, 28]. As for that between the sample holder and the screen coordinate system, a rotation around ***Z_{sh}***, denoted γ^M exists composed of a magnetic rotation induced by the electromagnetic lens (magnification dependent) and a rotation related to the specific sample loading axis. For the TEMs, γ^M has been corrected by the imaging system (for most modern TEMs), the screen and the sample holder coordinate system coincide when no tilt is applied (Fig. 1). However, when γ^M is not corrected, the orientation relation can be described by (γ^M, 0, 0) (Fig. 1).

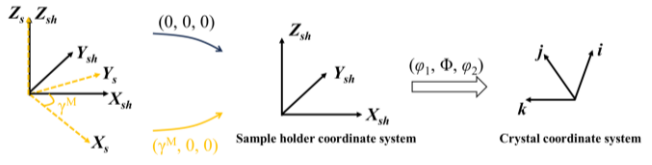

Figure 1. *Schematic diagram of orientation relations between three coordinate systems. γ^M is non-corrected magnetic rotation angle.*

For any crystal system, the structure can be represented by the Bravais lattice and the lattice cell is defined by its lattice constants (a, b, c, α, β and γ) (denoted Bravais lattice basis (***a-b-c***) in the present work). As the crystalline directions and planes are expressed with the Miller Indices, equivalent to the coordinates expressed in the Bravais lattice basis for the former and in its reciprocal space for the latter, the geometrical relation between the orthonormal crystal coordinate system (***i-j-k***) and the Bravais lattice basis should be resolved. There are two ways to set the orthonormal crystal coordinate system with respect to the Bravais lattice basis, one being with ***i//a*** and ***k//a×b*** and the other ***j//b*** and ***k//a×b***. Thus, the coordinate transformation matrix from (***i-j-k***) to (***a-b-c***) can be resolved. A detailed deduction is given in **Appendix 1**.

2.2. Stereographic projection in sample holder coordinate system

Stereographic projection is commonly used to visualize the orientation of any crystalline vectors and their angular relations. Fig. 2a illustrates the stereographic projection of a vector ***g*** (could be a reflection vector) on the equatorial plane ***X_{sh}-O-Y_{sh}***. P (x, y, z) is the intersection of ***g*** (unit vector) on the surface of the unit projection sphere ***O- $X_{sh}Y_{sh}Z_{sh}$***. P' (x', y'), the intersection of the line connecting P and the south pole S with the ***X_{sh}-O-Y_{sh}*** plane, is the stereographic projection or the pole of ***g***. The detailed formulation for the calculations is well documented and can be found, for example, in [31].

To project a crystalline vector or a plane normal vector in the sample holder coordinate system, the vector is needed to be expressed in the sample holder coordinate system. This can be done through coordinate transformation from the Bravais lattice basis (***a-b-c***) (for a vector with Miller indices [u v w]) or from the reciprocal space of the Bravais lattice basis (***a*-b*-c****) (for plane normal vector with plane indices (h k l)) to the sample holder coordinate system via the orthonormal crystal coordinate system (***i-j-k***). Using the determined crystal orientation (φ_1, Φ, φ_2) and considering crystal symmetry, the transformation of all the equivalent vectors by symmetry can be described:

$$\overrightarrow{v_{B\to sh}} = M_E \cdot S_i \cdot M_{C\to B} \cdot \overrightarrow{v_B}, \quad (1)$$

where M_E (Eq. A19 in **Appendix 2**) is the coordinate transformation matrix between the sample coordinate system and the orthonormal crystal coordinate system linked with the Euler angles (φ_1, Φ, φ_2), S_i (i = 1 - n, n depending on crystal symmetry) the rotational symmetry matrices, $M_{C\to B}$ the coordinate transformation matrix from the orthonormal crystal coordinate system to the Bravais lattice basis (**Appendix 1**), and $\overrightarrow{v_B}$ and $\overrightarrow{v_{B\to sh}}$ are vectors expressed in the Bravais lattice basis and the sample holder coordinate system, respectively. For the normal vector to (hkl) plane, $\overrightarrow{v_B} = G_{ij}^* \cdot \overrightarrow{n_{hkl}^*}$ (G_{ij}^* the reciprocal metric tensor: Eq. A2 and n_{hkl}^* the normal vector to the plane: **Appendix 1**). Thus, the geometrical relations between the projection pole (P'), the screen coordinate system (***X_s-Y_s-Z_s***), the sample holder coordinate system (***X_{sh}-Y_{sh}-Z_{sh}***) and the electron beam (***EB***) are defined, as illustrated in Fig. 2b and c.

2.3. To achieve two-beam/weak beam condition

With the resolved geometrical relation between the electron beam, vector ***g*** representing the reflection plane and the sample holder rotation/tilt axes, to reach the two-beam condition of ***g*** can be guided by rotating or tilting the sample holder. To this end, first, the screen coordinate system that is fixed is chosen as the reference for the stereographic projection during sample holder tilt operations. For clarity, we denote it ***X-Y-Z***, and for simplicity, we consider that the magnetic rotation γ^M is corrected. Under this condition, the sample holder coordinate system (***X_{sh}-Y_{sh}-Z_{sh}***) coincides with the screen coordinate system (***X-Y-Z***) when no tilt is applied.

There are two commonly used double tilt systems: **α** tilt (around the ***X*** axis of the holder) + **γ** rotation (around the ***Z*** axis) and the **α** tilt + **β** tilt (around the ***Y*** axis). According to the mechanical systems of the two kinds of sample holders, the **α** tilt articulates the ***Y*** and ***Z*** axes, whereas the **γ** rotation or **β** tilt is independent and will not affect the other two holder axes. Based on such a characteristic, we propose to apply the **γ** rotation or **β** tilt first and the **α** tilt second to facilitate the operation process, if tilt or rotation along two holder axes are required. Here all the rotation or tilt operations follow the right

Permanent link http://www.atex-software.eu/papers/ATEX_TEM_Aligner_Paper.pdf
D O I https://doi.org/10.1107/S1600576725010118

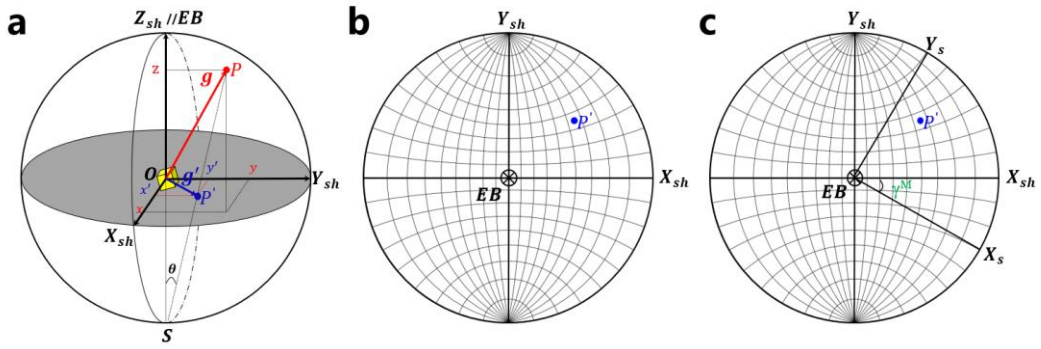

Figure 2. *Illustration of stereographic projection in sample holder coordinate system. (a) 3D illustration; (b) and (c) pole figure presentation showing geometrical relation between projection pole (P'), screen coordinate system (**X_s-Y_s-Z_s**), sample holder coordinate system (**X_{sh}-Y_{sh}-Z_{sh}**) and electron beam (**EB**) with and without rotation correction.*

handedness. Also, to facilitate the rotation angle calculations, we suggest to use different projection planes for the operations with the two different holder systems, as detailed in the next part. It should also be noted that in practical TEM operations the sample holder rotations/tilts are constrained by angular limits for image quality or availability.

For the α tilt + γ rotation sample holder, the ***X-O-Y*** plane is selected as the projection plane, as shown in Fig. 3 where the angular limits for γ rotation (unlimited) and **α** tilt (±40° for example) are shaded in gray (Fig. 3a$_2$) and blue (Fig. 3b$_2$), respectively. In the figures, $\boldsymbol{g}$ is the unit vector representing the reflection plane expressed in the sample holder coordinate system, and P is the projection pole of $\boldsymbol{g}$. The two-beam condition for this reflection corresponds to moving its projection pole to the grand cycle of the ***X-O-Y*** projection plane where the reflection plane of $\boldsymbol{g}$ is parallel to the transmitted beam i.e., the transmitted beam and the reflected beam $\boldsymbol{g}$ are on-edge (two-beam condition). To this end, the general operation process could be realized by two steps, a **γ** rotation plus an **α** tilt. Firstly, **γ** rotation: the **γ** rotation around the ***Z*** axis moves $\boldsymbol{g}$ to $\boldsymbol{g}'$ (Fig. 3a$_1$), correspondingly its pole P to P' (Fig. 3a$_1$ and a$_2$). After that, $\boldsymbol{g}$ is on the ***Y-O-Z*** plane and its projection is on the ***Y*** axis. Secondly, **α** tilt: the **α** tilt around the ***X*** axis moves $\boldsymbol{g}'$ to $\boldsymbol{g}''$ (Fig. 3a$_1$) and, correspondingly, its pole P' to P'' (Fig. 3a$_1$ and a$_2$). After the two steps, vector $\boldsymbol{g}$ is parallel to the ***Y*** axis and the corresponding reflection plane is parallel to the transmitted beam, reaching the two-beam condition. In this operation, γ is defined by the angle between ***OP*** and the ***Y*** axis and α is defined by the angle between $\boldsymbol{g}'$ and the ***Y*** axis, equivalent to that between ***OP*** and $\boldsymbol{g}$, as illustrated in Fig. 3a$_1$. Alternatively, a single **α** tilt to reach the two-beam condition is also possible, as shown in Fig. 3b. In this case, the projection pole of $\boldsymbol{g}$ should be located within the α limit (the blue zone in Fig. 3b$_2$). Then, α is defined by the angle between $\boldsymbol{g}$ and $\boldsymbol{g}'$. It should be noted that, as the tilt is around the ***X*** axis, the angles of $\boldsymbol{g}$ and $\boldsymbol{g}'$ with the ***X*** axis are equal. Thus, the coordinates of $\boldsymbol{g}'$ can be calculated using the angle between $\boldsymbol{g}$ and the ***X*** axis. The detailed information

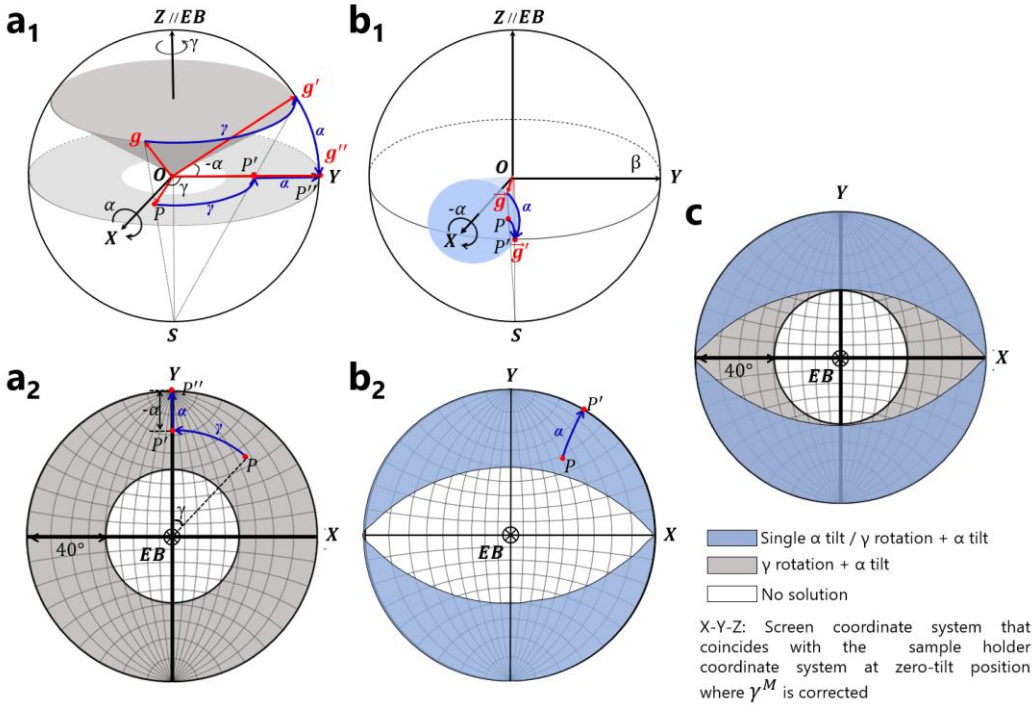

Figure 3. *3D schematic diagrams and pole figure representations illustrating (a) two step sample rotations and (b) single α tilt to achieve two-beam condition using a **α** tilt + **γ** rotation TEM sample holder system with shaded zones indicating sample holder rotation and tilt limits and pole figure representation (c) highlighting orientation zones for different operations.*

Permanent link http://www.atex-software.eu/papers/ATEX_TEM_Aligner_Paper.pdf
D O I https://doi.org/10.1107/S1600576725010118

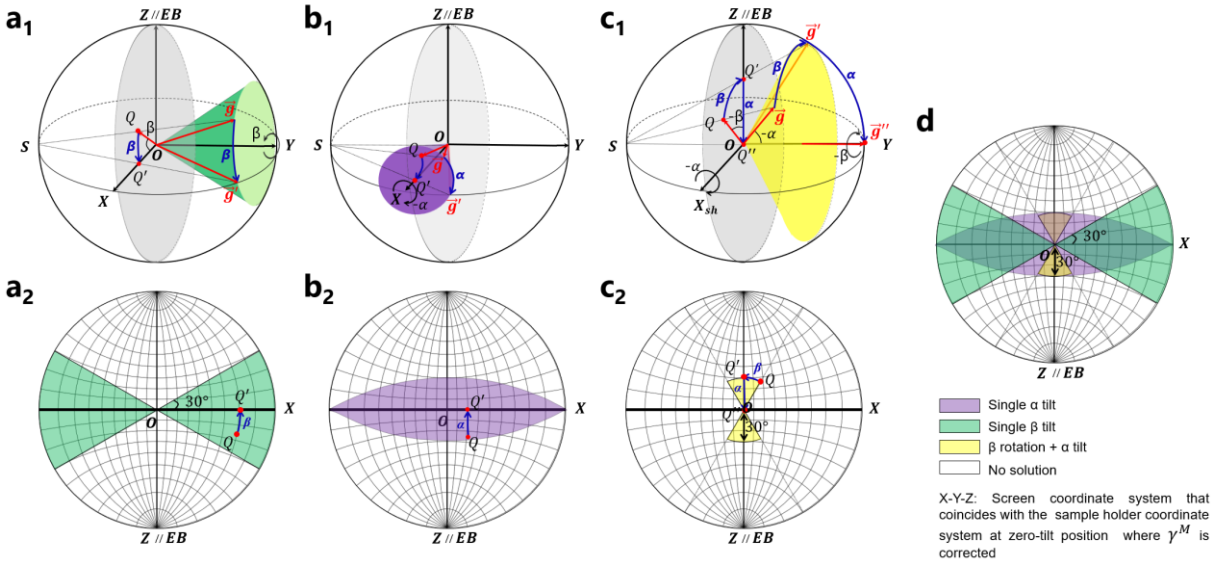

Figure 4. *3D schematic diagrams and pole figure representations illustrating (a) single* ***β****, (b) single* ***α*** *and (c) two step sample tilts (****β*** *+* ***α****) to reach two beam condition using* ***β*** *tilt +* ***α*** *tilt TEM sample holder system with shaded zones indicating sample holder tilt limits and (d) pole figure representation highlighting orientation zones for different operations. In figures, ±30° for both* ***α*** *tilt and* ***β*** *tilt is assumed.*

for the vector coordinates and the rotation and tilt angle calculation formulae are given in Table 1. As a summary, Fig. 3c highlights the orientation zones for the corresponding operations to achieve the two-beam condition, using the **α** tilt + **γ** rotation sample holder.

For the α tilt + β tilt sample holder, the ***X-O-Z*** plane is selected as the projection plane, as shown in Fig. 4. The operation to the two-beam condition is to move the projection pole of ***g*** to the thick black horizontal line that represents the grand cycle of the ***X-O-Y*** plane. Similarly, the **α** tilt + **β** tilt sample holder also has rotation angle limitations. Unlike the **α** tilt + **γ** rotation holder that has rotation limitation only along ***X***, the **α** tilt + **β** tilt holder has tilt limit along both the ***X*** and the ***Y*** axis.

Considering the tilt-limit of the **α** tilt + **β** tilt sample holder, the operation to obtain the two-beam position can be specified into three cases, single **β** tilt, single **α** tilt and **β** + **α** tilt. In the first case, when the angle between ***g*** and the ***X-O-Y*** plane is smaller than the tilt limit along the ***Y*** axis (**β** tilt), as shown in Fig. 4a$_1$ where the pole *Q* is in the green region, the two-beam position can be reached by a single **β** tilt (Fig. 4 a$_1$ and a$_2$). In this case, β is defined by the angle between ***OQ*** and ***OX***. In the second case where the angle between ***g*** and the ***X-O-Y*** plane is smaller than the tilt limit along the ***X*** axis (**α** tilt), as shown in Fig. 4b$_1$, and the pole of ***g*** falls in the purple region in Fig. 4b$_2$, the two-beam condition can be realized by a single **α** tilt. This case is the same as the single **α** tilt using the **α** tilt + **γ** rotation sample holder, as described above. In the last case, the projection pole of ***g*** falls in the yellow region in Fig. 4c$_1$ and c$_2$. To reach the two-beam condition, two steps of rotations are required, **β** tilt + **α** tilt. Firstly, **β** tilt: the **β** tilt moves vector ***g*** to ***g***′ (on the ***Y-O-Z*** plane) (Fig. 4c$_1$), correspondingly its pole *Q* to *Q*′ (Fig. 4c$_2$). Secondly, **α** tilt, the **α** tilt further moves ***g***′ to ***g***″ (Fig. 4c$_1$), consequently *Q*′ to *Q*″ (Fig. 4c$_2$), to the two-beam condition (Fig. 4c$_2$). Here, β corresponds to the angle between ***OQ*** and ***OZ***, whereas α to the angle between ***g*** and ***OY***. The angle calculations are in Table 1. Fig. 4d shows the summary of all possible orientation regions of ***g*** that can reach the two-beam conditions.

Table 1. *Calculation of tilt and rotation angles for operations to reach two-beam conditions using different sample holder systems*

Holder	Rotation	Vector (with $g\ (x, y, z)$ for all cases)		Equation	Result
α tilt + γ rotation	**γ + α**	$\boldsymbol{OP}_{unit}$ $\left(\frac{x}{\sqrt{x^2+y^2}}, \frac{y}{\sqrt{x^2+y^2}}, 0\right)$	$\boldsymbol{OY}_{sh}\ (0,1,0)$	$\gamma = \cos^{-1}(\boldsymbol{OP}_{\text{unit}} \cdot \boldsymbol{OY}_{sh})$ $\alpha = \cos^{-1}(\boldsymbol{OP}_{\text{unit}} \cdot \boldsymbol{g})$	$\gamma = \cos^{-1}(y/\sqrt{x^2+y^2})$ $\alpha = \cos^{-1}(\sqrt{x^2+y^2})$
	α	$\boldsymbol{g}'\ (x, \sqrt{1-x^2}, 0)$		$\alpha = \cos^{-1}(\boldsymbol{g} \cdot \boldsymbol{g}')$	$\alpha = \cos^{-1}(x^2 + y\sqrt{1-x^2})$
α tilt + β tilt	**β**	$\boldsymbol{OQ}_{\text{unit}}$ $\left(\frac{x}{\sqrt{x^2+z^2}}, 0, \frac{z}{\sqrt{x^2+z^2}}\right)$	$\boldsymbol{OX}_{sh}\ (1,0,0)$	$\beta = \cos^{-1}(\boldsymbol{OQ}_{unit} \cdot \boldsymbol{OX}_{sh})$	$\beta = \cos^{-1}\left(x/\sqrt{x^2+z^2}\right)$
	β + α		$\boldsymbol{OZ}_{sh}\ (0,0,1)$ $\boldsymbol{OY}_{sh}\ (0,1,0)$	$\beta = \cos^{-1}(\boldsymbol{OQ}_{\text{unit}} \cdot \boldsymbol{OZ}_{sh})$ $\alpha = \cos^{-1}(\boldsymbol{OY}_{sh} \cdot \boldsymbol{g})$	$\beta = \cos^{-1}\left(z/\sqrt{x^2+z^2}\right)$ $\alpha = \cos^{-1}(y)$
	α	$\boldsymbol{g}'\ (x, \sqrt{1-x^2}, 0)$		$\alpha = \cos^{-1}(\boldsymbol{g} \cdot \boldsymbol{g}')$	$\alpha = \cos^{-1}(x^2 + y\sqrt{1-x^2})$

Permanent link http://www.atex-software.eu/papers/ATEX_TEM_Aligner_Paper.pdf
D O I https://doi.org/10.1107/S1600576725010118

2.4. To achieve zone-axis on-edge condition

Different from the two-beam operation, the zone-axis on-edge condition is to tilt/rotate the sample so that a desired zone-axis is parallel to the beam. Similar to the two-beam operation, different projection planes are used for different sample holder systems.

For the α tilt + γ rotation sample holder, the ***X-O-Y*** plane is selected as the projection plane, as shown in Fig. 5. The operation to reach the zone-axis on-edge condition is to move the projection pole of the zone-axis vector $\boldsymbol{v}$ to the center of the ***X-O-Y*** plane (Fig. 5b) that represents the incident electron beam. This can be achieved by a two-step sample operation: **γ** rotation + **α** tilt. The **γ** rotation around the ***Z*** axis moves $\boldsymbol{v}$ in Fig. 5a to $\boldsymbol{v}'$ (to the ***Y-O-Z*** plane), correspondingly, its pole *p* in Fig. 5a and b to *p*′. Then, the **α** tilt around the ***X*** axis takes $\boldsymbol{v}'$ to $\boldsymbol{v}''$ (Fig. 5a) that is parallel to the incident beam ***EB***, (the on-edge condition), correspondingly the pole *p*′ to *p*′′ (Fig. 5b) (the center of the ***X-O-Y*** plane). The angle γ is defined by ***op*** and ***OY*** and α by $\boldsymbol{v}$ and ***OZ***. The angle calculations are given in Table 2.

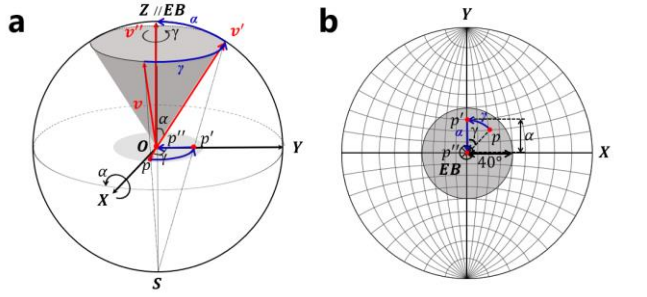

Figure 5. *3D schematic diagram (a) and pole figure representation (b) illustrating two step sample tilts (**γ** + **α**) to reach zone-axis on-edge condition using **γ** rotation + **α** tilt TEM sample holder system with shaded zones (b) indicating sample holder tilt limit.*

For the α tilt + β tilt sample holder, the ***X-O-Z*** plane is selected as the projection plane, as shown in Fig. 6. The operation is to move the zone-axis $\boldsymbol{v}$ to the ***OZ*** axis that represents the beam direction. Thus, the first step is the **β** tilt around the ***OY*** axis, which moves $\boldsymbol{v}$ to $\boldsymbol{v}'$ (Fig. 6a) to the ***Y-O-Z*** plane. Correspondingly, the pole *q* moves to *q*′(Fig. 6a and b). The second step is the **α** tilt around the ***OX*** axis, which rotates $\boldsymbol{v}'$ to $\boldsymbol{v}''$ **(**to be parallel to the incident beam direction**)** (Fig. 6a), correspondingly the pole *p*′ to *p*′′ (Fig. 6b). The angle β is defined by ***oq*** and ***OZ*** and α by ***oq*** and $\boldsymbol{v}$. The angle calculations are given in Table 2.

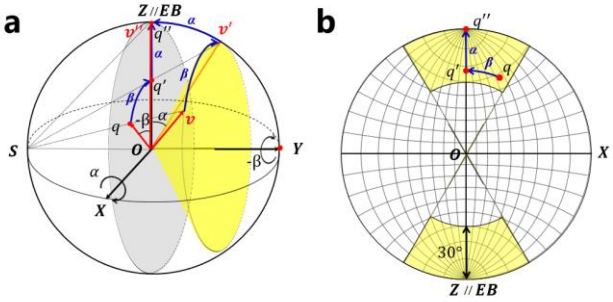

Figure 6. *3D schematic diagram (a) and pole figure representation (b) illustrating two step sample tilts (**β** + **α**) to reach zone-axis on-edge condition using **β** tilt + **α** tilt TEM sample holder system with shaded zones (b) indicating sample holder tilt limit.*

A software module "TEM-Aligner" is developed for all the crystal systems and integrated in the open-source software package – *Analysis Tools for Electron and X-ray diffraction, ATEX-software* [28]. The workflow of the Atex Software© module "TEM-Aligner" is presented in Appendix 3 (Fig. A3).

3. Application

Two examples are presented to illustrate the application of the developed approach. The material used is the $Co_{66.66}Cr_{16.67}V_{16.67}$ medium entropy alloy [32] and composed of a single FCC phase. The sample was annealed to defect-free state (1200 °C for 3 minutes) and then deformed to 2 % elongation by uniaxial tensile experiment. The TEM samples were mechanically thinned to ~100 μm in thickness and then electrolytically polished in a solution of 10 % $HClO_4$ and 90 % C_2H_5OH at a voltage of 12 V and at a temperature between 268 and 273 K. The TEM used is Philips CM200 (without magnetic rotation correction) equipped with an α tilt + γ rotation sample holder and the home-made orientation determination software *Euclid Phantasies (EP)* [26]. In Example 1, the two-beam condition was used to determine the Burgers vector of the partial dislocations bordering the stacking faults, and, in Example 2, the [112] zone-axis on-edge condition was obtained to visualize the chemically ordered-domains reported in the literature [33-35].

Table 2. *Calculation of tilt and rotation angles for operations to reach zone-axis on-edge condition using different sample holder systems. Vector v, the zone-axis, is a unit vector.*

Holder	Rotation	Vector (with $v\ (x,y,z)$ for all cases)		Equation	Result
α tilt + γ rotation	**γ + α**	$\boldsymbol{Op}_{unit}$ $\left(\frac{x}{\sqrt{x^2+y^2}},\frac{y}{\sqrt{x^2+y^2}},0\right)$	$\boldsymbol{OY}_{sh}\ (0,1,0)$ $\boldsymbol{OZ}_{sh}\ (0,0,1)$	$\gamma=\cos^{-1}(\boldsymbol{Op}_{\mathrm{unit}}\cdot\boldsymbol{OY}_{sh})$ $\alpha=\cos^{-1}(\boldsymbol{v}\cdot\boldsymbol{OZ}_{sh})$	$\gamma=\cos^{-1}(y/\sqrt{x^2+y^2})$ $\alpha=\cos^{-1}(z)$
α tilt + β tilt	**β + α**	$\boldsymbol{Oq}_{\mathrm{unit}}$ $\left(\frac{x}{\sqrt{x^2+z^2}},0,\frac{z}{\sqrt{x^2+z^2}}\right)$	$\boldsymbol{OZ}_{sh}\ (0,0,1)$	$\beta=\cos^{-1}(\boldsymbol{Oq}_{\mathrm{unit}}\cdot\boldsymbol{OZ}_{sh})$ $\alpha=\cos^{-1}(\boldsymbol{Oq}_{\mathrm{unit}}\cdot\boldsymbol{v})$	$\beta=\cos^{-1}(z/\sqrt{x^2+z^2})$ $\alpha=\cos^{-1}(\sqrt{x^2+z^2})$

Permanent link http://www.atex-software.eu/papers/ATEX_TEM_Aligner_Paper.pdf
D O I https://doi.org/10.1107/S1600576725010118

Example 1: Two-beam condition

Fig. 7a$_1$ shows the bright field image of the deformed sample at zero-tilt position. The deformation produced a large number of stacking faults each bordered by a pair of partial dislocations piling up before the twin interfaces, as highlighted by the red ellipsoid. A Kikuchi pattern is acquired from the location of the green marker in Fig. 7a$_1$ and shown in Fig. 7a$_2$. The orientation (in Euler angles in Bunge notation [29]) of the crystal (Fig. 7a$_1$) was determined by indexing the Kikuchi pattern with the *EP* software [28] and shown in Fig. 7a$_2$.

Based on the orientation of the crystal, the {111} and {220} pole figures are plotted and shown in Fig. 7a$_3$ and a$_4$, as these planes are useful reflection planes to determine the Burgers vector of the partial dislocations. By trace analysis using the stacking fault fringes, we found that the slip plane of the partial dislocations are the $(\bar{1}11)$ plane, as evidenced by the parallelism of the fringe orientation (marked by the black line in Fig. 7a$_1$) and the $(\bar{1}11)$ plane trace (the black solid line in Fig. 7a$_3$), which indicates that 3 partial dislocations ($\pm\boldsymbol{b}_{\frac{1}{6}[211]}$, $\pm\boldsymbol{b}_{\frac{1}{6}[\bar{1}\,\bar{2}1]}$ and $\pm\boldsymbol{b}_{\frac{1}{6}[\bar{1}1\bar{2}]}$) could be those in Fig. 7a$_1$. To unambiguously determine the Burgers vectors, the two beam conditions of $\boldsymbol{g}_{11\bar{1}}$ and $\boldsymbol{g}_{2\bar{2}0}$ were considered and the produced characteristic contrasts of the partial dislocations are given in Table 3. As the poles of $(11\bar{1})$ and $(2\bar{2}0)$ are located within the single α tilt zones (Fig. 7a$_3$ and a$_4$ indicated in blue), the single α tilt was applied for either case. The two-beam conditions with the respective $\boldsymbol{g}_{11\bar{1}}$ and $\boldsymbol{g}_{2\bar{2}0}$ on edge were achieved after the respective α tilt. The bright-field images, the Kikuchi patterns and the pole figures corresponding to the two different tilted sample positions are updated in Fig. 7b and c. The contrast features (highlighted in bold in Table 3) generated by $\boldsymbol{g}_{11\bar{1}}$ and $\boldsymbol{g}_{2\bar{2}0}$ on-edge rules out the $\boldsymbol{b}_{\frac{1}{6}[211]}$ partial dislocation, and those produced by $\boldsymbol{g}_{2\bar{2}0}$ clearly differentiate the $\boldsymbol{b}_{\frac{1}{6}[\bar{1}\,\bar{2}1]}$ partial (weak; closer to the twin boundary) from the $\boldsymbol{b}_{\frac{1}{6}[\bar{1}1\bar{2}]}$ partial (strong, farther). This example validates the workability of the method and the software module. The corresponding snap-shorts of the software interfaces are shown in Fig. A4a and b in **Appendix 3**.

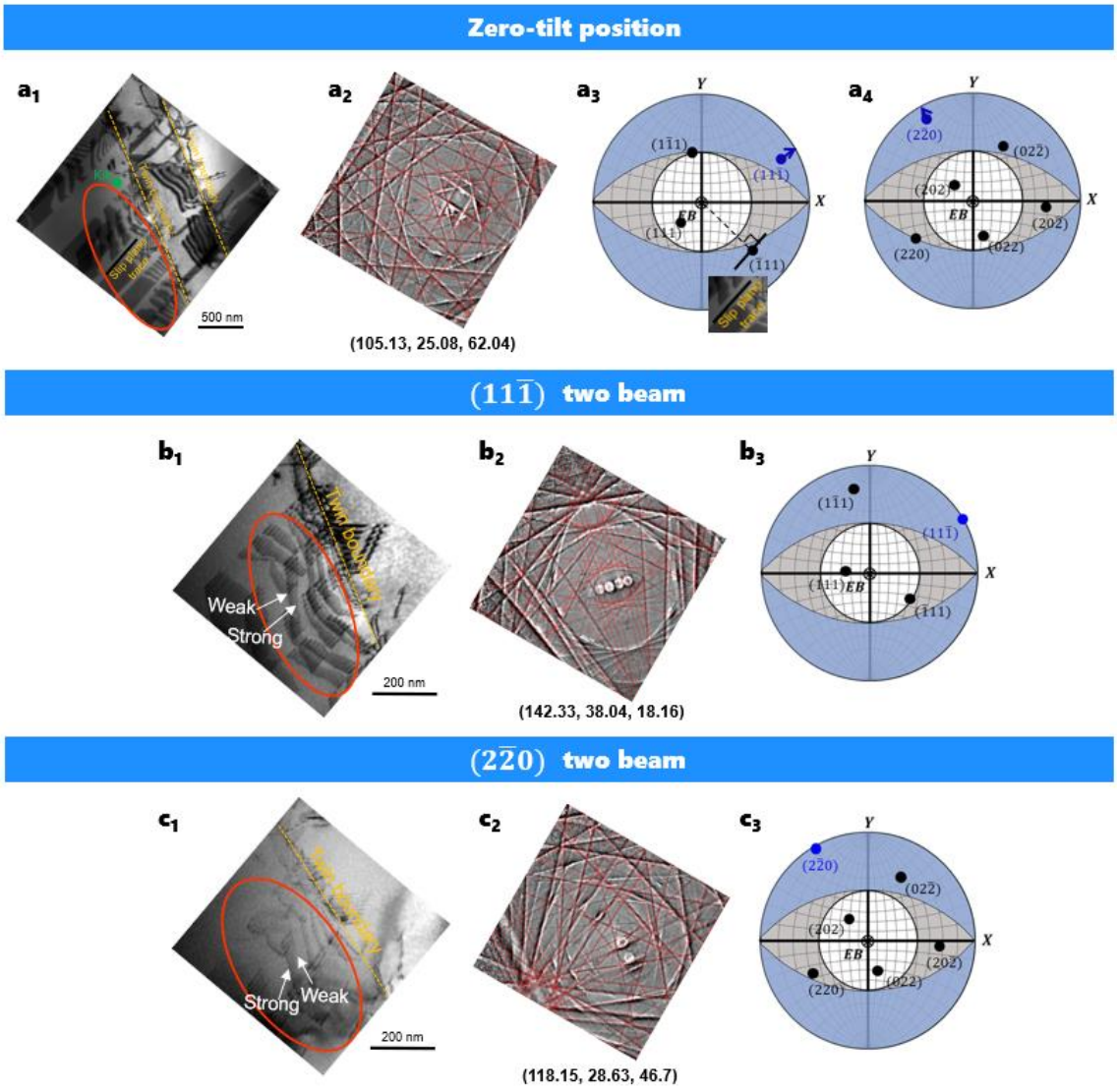

Figure 7. *(a1) Bright field image of stacking faults bordered with pairs of partial dislocations cycled in red in front of twin boundary, (a2) Kikuchi pattern obtained from point highlighted in green in (a1) and corresponding Euler angles (in Bunge notation (Bunge et al., 1981)) and (a3) & (a4) {1 1 1} and {2 2 0} pole figures of sample in zero-tilt position illustrating α tilt operations to reach two-beam conditions of reflections highlighted in blue in pole figures. (b1) & (c1) Bright field images of stacking faults with characteristic contrasts in two-beam conditions with $\boldsymbol{g}_{11\bar{1}}$ and $\boldsymbol{g}_{2\bar{2}0}$ on-edge, (b2) & (b3) and (c2) & (c3) updated Kikuchi patterns in tilt positions and corresponding {1 1 1} & {2 2 0} pole figures. Magnetic rotations in both imaging and diffraction states were corrected manually by rotating the respective images.*

Permanent link http://www.atex-software.eu/papers/ATEX_TEM_Aligner_Paper.pdf
D O I https://doi.org/10.1107/S1600576725010118

Example 2: Zone-axis on-edge

In this example, we used the <21$\bar{1}$> zone-axis for characterizing the presence of the chemically short-range ordered (CSRO) domains in the studied alloy. As reported in numerous previous investigations [35-37], the appearance of diffused diffraction spots at the 1/2{113} reflection positions are indicative for the existence of the CSRO domains. The {113} planes belong to the <21$\bar{1}$> axis-zone. Thus, the existence of the CSRO domains can be verified with the <21$\bar{1}$> zone-axis being on-edge, i.e., the beam is parallel to one of the <21$\bar{1}$> directions.

Fig. 8a$_1$ shows the bright field image of the sample obtained at zero-tilt position. A Kikuchi pattern corresponding to the green marker in Fig. 8a$_1$ is shown in Fig. 8a$_2$. The orientation (represented in the Euler angles in Bunge notation [29]) of the sample was obtained by indexing the Kikuchi pattern shown in Fig. 8 a$_2$. Based on the obtained Euler angles, the <21$\bar{1}$> pole figure was plotted, as shown in Fig. 8a$_3$. The [1$\bar{1}$2] direction possesses the smallest angular inclination from the incident beam direction (the center of the pole figure). The necessary rotation and tilt angles to bring the [1$\bar{1}$2] direction on edge were then calculated and listed in Table 5. After the corresponding γ rotation and α tilt operations, the [1$\bar{1}$2] on edge condition was reached, as shown by the new Kikuchi pattern, the Selected Area Election Diffraction (SAED) pattern and the pole figure in Figs. 8b$_3$ to b$_5$. In Fig. 8b$_4$, the diffraction spots of the CSRO are clearly visible at the ½ {131} positions despite the diffusivity, indicating the existence of the CSRO domains in the studied alloy. A large number of white domains in the dark field image in Fig. 8b$_1$ and magnified in Fig. 8b$_2$ produced using the diffracted beam at ½ (131) further manifest their size, morphology and the distribution. This example well illustrates the operation process to reach the zone-axis on-edge condition. The corresponding snap shot of the software interface is shown in Fig. A4c in **Appendix 3**.

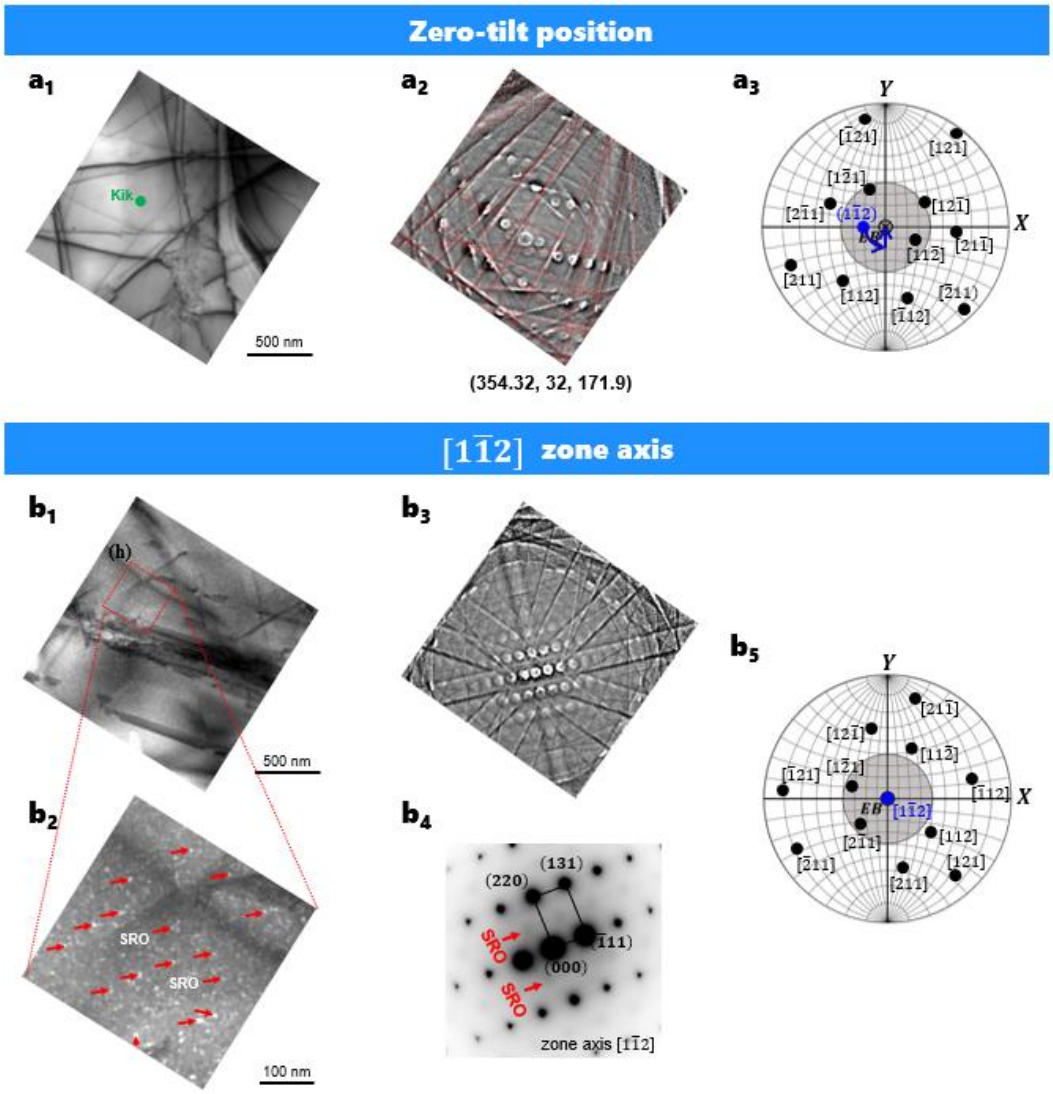

Figure 8. (a1) Bright field image acquired at zero-tilt sample holder position, (a2) Kikuchi pattern obtained from point highlighted in green in (a1) and its corresponding Euler angles (in Bunge notation [29]) and (a3) corresponding <1 1¯2> direction pole figure, illustrating rotation-tilt operations to reach zone-axis on edge. (b1) and (b2) Dark field images of CSRO domains at [1 1¯2] on-edge produced by ½ (131) diffracted beam in selected area electron diffraction (SAED) pattern (b4), (b3) Kikuchi pattern corresponding to tilt position, illustrating the beam condition of zone-axis on edge and (b5) <1 1¯2> direction pole figure showing [1 1¯2] on-edge.

Permanent link http://www.atex-software.eu/papers/ATEX_TEM_Aligner_Paper.pdf
D O I https://doi.org/10.1107/S1600576725010118

Summary

A novel method based on the determined crystallographic orientation of the crystals to directly achieve the desired beam orientation for imaging in TEM for a variety of analyses was elaborated and A dedicated software module ('TEM-Aligner') was developed and integrated in the home-made open-source software package – *Analysis Tools for Electron and X-ray diffraction, ATEX-software*. The method leverages the crystallographic orientation determination of the subject crystal and progresses with a maximum two-step sample rotation guided by the determined orientation to reach the two-beam condition for defect imaging and the zone-axis on-edge condition for a large span of analyses from precipitation of secondary phases, crystallographic orientation relationship, crystal structure determination to atomic arrangements, using both the conventional TEM and the state-of-the-art high resolution TEM/STEM. The method has two great impacts. First, it replaces the conventional search through trial-and-error by a precisely defined process, thus greatly saving the man-machine effort and time that are extremely expensive. Second, it can be of interest also for TEM producers by programing automatic sample holder rotation/tilt to further facilitated the beam orientation optimization that represents as one of the toughest TEM tasks.

Acknowledgements

We acknowledge the experimental facilities MécaRhéo | MicroMat | Procédés from LEM3 (Université de Lorraine-CNRS UMR 7239).

References

[1] K. H. Katerbau, Philos. Mag. A 43(2), 409–426 (2006). https://doi.org/10.1080/01418618108239418

[2] D. J. H. Cockayne, Z. Naturforsch. A 27a, 452–460 (1972). https://doi.org/10.1515/zna-1972-0313

[3] T. Waitz, V. Kazykhanov and H. P. Karnthaler, Acta Mater. 52(1), 137–147 (2004). https://doi.org/10.1016/j.actamat.2003.08.036

[4] J. Liu, C. Chen, Q. Feng, X. Fang, H. Wang, F. Liu, J. Lu and D. Raabe, Mater. Sci. Eng. A 703, 236–243 (2017). https://doi.org/10.1016/j.msea.2017.06.107

[5] Y. Zhong, Y. Yuan, H. Li, S. Xu, Y. Xi and X. Wang, Acta Mater. 294, 121094 (2025). https://doi.org/10.1016/j.actamat.2025.121094

[6] H. Jin, J. Zhang, Y. Zhang, W. Zhang, S. Ma, S. Mao, Y. Du, Z. Wang, J. Qin and Q. Wang, Mater. Charact. 183, 111609 (2022). https://doi.org/10.1016/j.matchar.2022.111609

[7] O. Molnárová, M. Klinger, J. Duchoň, H. Seiner and P. Šittner, Acta Mater. 258, 119242 (2023). https://doi.org/10.1016/j.actamat.2023.119242

[8] J. Li, M. Zhang, C. Zhang and J. Han, Scr. Mater. 265, 116719 (2025). https://doi.org/10.1016/j.scriptamat.2025.116719

[9] M. De Graef, Introduction to Conventional Transmission Electron Microscopy, Cambridge University Press, Cambridge (2003), pp. 345–394.

[10] J.-K. Kim and B. C. De Cooman, Scr. Mater. 128, 78–82 (2017). https://doi.org/10.1016/j.scriptamat.2016.12.045

[11] J. Liu, C. Chen, Y. Xu, S. Wu, G. Wang, H. Wang, Y. Fang and L. Meng, Scr. Mater. 137, 9–12 (2017). https://doi.org/10.1016/j.scriptamat.2017.04.004

[12] M. E. van Dalen, D. C. Dunand and D. N. Seidman, Acta Mater. 53(15), 4225–4235 (2005). https://doi.org/10.1016/j.actamat.2005.05.006

[13] S. Kondo, N. Shibata and Y. Ikuhara, Scr. Mater. 258, 116513 (2025). https://doi.org/10.1016/j.scriptamat.2024.116513

[14] L. Wang, X. Liang, B. Liu, M. Oehring, J. Paul, J. Liu, M. Song, F. Pyczak and Y. Liu, Scr. Mater. 222, 115034 (2023). https://doi.org/10.1016/j.scriptamat.2022.115034

[15] C. Zhang, Y. Wu, L. You, W. Qiu, Y. Zhang, Y. Yuan, Z. Lu and X. Song, Scr. Mater. 178, 503–507 (2020). https://doi.org/10.1016/j.scriptamat.2019.11.016

[16] P. Wu, Y. Zhang, L. Han, K. Gan, D. Yan, W. Wu, L. He, Z. Fu and Z. Li, Acta Mater. 261, 119389 (2023). https://doi.org/10.1016/j.actamat.2023.119389

[17] Q. Pan, M. Yang, R. Feng, A. C. Chuang, K. An, P. K. Liaw, X. Wu, N. Tao and L. Lu, Science 382(6667), 185–190 (2023). https://doi.org/10.1126/science.adf4015

[18] Z. Liu, P. Ma, Y. Jiang, F. Cao, Y. Zhang and C. Liu, Acta Mater. 283, 120535 (2025). https://doi.org/10.1016/j.actamat.2024.120535

[19] P. Humble, Phys. Status Solidi B 30(1), 183–192 (1968). https://doi.org/10.1002/pssb.19680300120

[20] P. Humble, Diffraction and Imaging Techniques in Materials Science, North-Holland, Amsterdam (1970).

[21] A. K. Head, P. Humble, L. M. Glarebrough, A. J. Morton and C. T. Forwood, Computed Electron Micrographs and Defect Identification, North-Holland, Amsterdam (1973).

[22] M. De Graef, Introduction to Conventional Transmission Electron Microscopy, Cambridge University Press, Cambridge (2003).

[23] R. A. Schwarzer, Ultramicroscopy 67(1), 19–24 (1997). https://doi.org/10.1016/S0304-3991(96)00113-6

[24] R. A. Schwarzer and S. Zaefferer, Int. J. Mater. Res. 38, 585–591 (1994).

[25] A. Morawiec, J. Appl. Crystallogr. 32, 788–798 (1999). https://doi.org/10.1107/S002188989900153X

[26] A. Morawiec, J.-J. Fundenberger, E. Bouzy and E. Lecomte, J. Appl. Crystallogr. 35, 287 (2002). https://doi.org/10.1107/S0021889802002925

[27] Nanomegas, TEM Orientation Imaging – ASTAR.

[28] B. Beausir and J.-J. Fundenberger, Analysis Tools for Electron and X-ray Diffraction, ATEX-software, Université de Lorraine – Metz (2017).

[29] H. Bunge, C. Esling and J. J. F. Muller, Found. Adv. 37(6), 889–899 (1981).

[30] Y. Zhang, S. Wang, C. Esling, J.-S. Lecomte, C. Schuman, X. Zhao and L. Zuo, J. Appl. Crystallogr. 44(6), 1164–1168 (2011). https://doi.org/10.1107/S0021889811041530

[31] H. Liu and J. Liu, J. Appl. Crystallogr. 45(1), 130–134 (2012). https://doi.org/10.1107/S0021889811052877

[32] L. Wang, H.-L. Yan, Y. Zhang, B. Beausir, W. Gan, P. Laurent, N. Siredey-Schwaller, C. Esling, X. Zhao and L. Zuo, Int. J. Plast. 186, 104260 (2025). https://doi.org/10.1016/j.ijplas.2024.104260

[33] L. Li, Z. Chen, S. Kuroiwa, M. Ito, K. Yuge, K. Kishida, H. Tanimoto, Y. Yu, H. Inui and E. P. George, Acta Mater. 243, 118537 (2023). https://doi.org/10.1016/j.actamat.2022.118537

[34] R. Zhang, S. Zhao, J. Ding, Y. Chong, T. Jia, C. Ophus, M. Asta, R. O. Ritchie and A. M. Minor, Nature 581, 283–287 (2020). https://doi.org/10.1038/s41586-020-2275-z

[35] X. Chen, Q. Wang, Z. Cheng, M. Zhu, H. Zhou, P. Jiang, L. Zhou, Q. Xue, F. Yuan, J. Zhu, X. Wu and E. Ma, Nature 592, 712–716 (2021). https://doi.org/10.1038/s41586-021-03345-9

Appendix 1

With the constants (a, b, c, α, β and γ) of the Bravais lattice, the direct space of the lattice cell and its reciprocal space can be explicitly defined with the basis vectors $\boldsymbol{a}$, $\boldsymbol{b}$ and $\boldsymbol{c}$ for the former and the basis vectors $\boldsymbol{a}^*$, $\boldsymbol{b}^*$ and $\boldsymbol{c}^*$ for the latter. The two spaces are related with each other with the geometrical relations $\boldsymbol{a}^* = \frac{\boldsymbol{b}\times\boldsymbol{c}}{V}$; $\boldsymbol{b}^* = \frac{\boldsymbol{c}\times\boldsymbol{a}}{V}$; $\boldsymbol{c}^* = \frac{\boldsymbol{a}\times\boldsymbol{b}}{V}$ with $V = \boldsymbol{a}\cdot(\boldsymbol{b}\times\boldsymbol{c})$. Thus, the metric tensors of the respective direct space (G_{ij}) and its reciprocal space (G^*_{ij}) can be resolved, as shown in Eqs. A1 and A2. It should be noted that the two spaces are dual and reciprocal to each other.

$$G_{ij} = \begin{bmatrix} g_{11} & g_{12} & g_{13} \\ g_{21} & g_{22} & g_{23} \\ g_{31} & g_{32} & g_{33} \end{bmatrix} = \begin{bmatrix} a^2 & ab\cos\gamma & ac\cos\beta \\ ab\cos\gamma & b^2 & bc\cos\alpha \\ ac\cos\beta & bc\cos\alpha & c^2 \end{bmatrix} \quad A1$$

$$G^*_{ij} = \begin{bmatrix} g^*_{11} & g^*_{12} & g^*_{13} \\ g^*_{21} & g^*_{22} & g^*_{23} \\ g^*_{31} & g^*_{32} & g^*_{33} \end{bmatrix} =$$

$$\begin{bmatrix} \frac{b^2c^2\sin^2\alpha}{V^2} & \frac{abc^2(\cos\alpha\cos\beta-\cos\gamma)}{V^2} & \frac{ab^2c(\cos\alpha\cos\gamma-\cos\beta)}{V^2} \\ \frac{abc^2(\cos\alpha\cos\beta-\cos\gamma)}{V^2} & \frac{a^2c^2\sin^2\beta}{V^2} & \frac{a^2bc(\cos\beta\cos\gamma-\cos\alpha)}{V^2} \\ \frac{ab^2c(\cos\alpha\cos\gamma-\cos\beta)}{V^2} & \frac{a^2bc(\cos\beta\cos\gamma-\cos\alpha)}{V^2} & \frac{a^2b^2\sin^2\gamma}{V^2} \end{bmatrix} \quad A2$$

Following the fundamental laws of the dual space, the vector $\boldsymbol{n}^*$ normal to the plane Miller indexed $(h\,k\,l)$ in the direct space is the vector in the reciprocal space with the same indices as the coordinates, i.e., $\boldsymbol{n}^* = \mathrm{h}\boldsymbol{a}^* + \mathrm{k}\boldsymbol{b}^* + \mathrm{l}\boldsymbol{c}^*$. The coordinate transformation of a vector between the two spaces are operated following the equations below:

$$\boldsymbol{v} = G^*_{ij}\boldsymbol{v}^* \quad A3$$

and

$$\boldsymbol{v}^* = G_{ij}\boldsymbol{v}, \quad A4$$

where $\boldsymbol{v}$ and $\boldsymbol{v}^*$ are the same vector expressed in the respective direct and reciprocal space. The scalar product of two vectors $\boldsymbol{p}(p_1,\ p_2,\ p_3)/\boldsymbol{p}^*(p^*_1,\ p^*_2,\ p^*_3)$ and $\boldsymbol{q}(q_1,\ q_2,\ q_3)/\boldsymbol{q}^*(q^*_1,\ q^*_2,\ q^*_3)$ in both direct and reciprocal spaces is:

$$\boldsymbol{p}\cdot\boldsymbol{q} = p_iG_{ij}q_j \quad (i,j\ =\ 1,2,3), (\text{In direct space}) \quad A5a$$

$$\boldsymbol{p}^*\cdot\boldsymbol{q}^* = p^*_iG^*_{ij}q^*_j \quad (i,j\ =\ 1,2,3), (\text{In reciprocal space}) \quad A5b$$

and the angle θ between $\boldsymbol{p}/\boldsymbol{p}^*$ and $\boldsymbol{q}/\boldsymbol{q}^*$ is:

$$\theta = cos^{-1}\left(\frac{p_iG_{ij}q_j}{\sqrt{p_iG_{ij}p_j}\sqrt{q_iG_{ij}q_j}}\right) \quad (\text{In direct space}) \quad A6a$$

$$\theta = cos^{-1}\left(\frac{p^*_iG^*_{ij}q^*_j}{\sqrt{p^*_iG^*_{ij}p^*_j}\sqrt{q^*_iG^*_{ij}q^*_j}}\right) \quad (\text{In reciprocal space}) \quad A6b$$

The cross product of two vectors $\boldsymbol{p}(p_1,\ p_2,\ p_3)$ and $\boldsymbol{q}(q_1,\ q_2,\ q_3)$ brings the resultant vector to its reciprocal space and vice versa:

$$\boldsymbol{p}\times\boldsymbol{q}//(p_2q_3 - p_3q_2)\boldsymbol{a}^* + (p_3q_1 - p_1q_3)\boldsymbol{b}^* + (p_1q_2 - p_2q_1)\boldsymbol{c}^* \quad (\text{direct space}) \quad A7a$$

$$\boldsymbol{p}^*\times\boldsymbol{q}^*//(p^*_2q^*_3 - p^*_3q^*_2)\boldsymbol{a} + (p^*_3q^*_1 - p^*_1q^*_3)\boldsymbol{b} + (p^*_1q^*_2 - p^*_2q^*_1)\boldsymbol{c} \quad (\text{reciprocal space}) \quad A7b$$

With these fundamental relations, the transformation matrix between the orthonormal crystal coordinate system and the Bravais lattice basis M_{C-B} (Fig. A1) expressed in Eq. A8 and 9 can be deduced. In the following deduction, the two different settings of the two coordinate systems are considered separately.

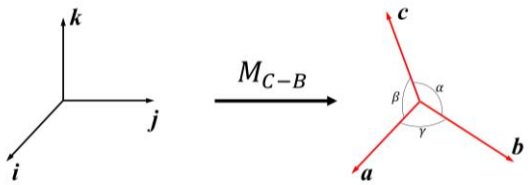

Figure A1. *Schema illustrating relation between orthonormal crystal coordinate system and Bravais lattice basis*

$$M_{C-B} = \begin{bmatrix} m_{11} & m_{12} & m_{13} \\ m_{21} & m_{22} & m_{23} \\ m_{31} & m_{32} & m_{33} \end{bmatrix} \quad A8$$

and

$$\begin{aligned} \boldsymbol{a} &= m_{11}\boldsymbol{i} + m_{21}\boldsymbol{j} + m_{31}\boldsymbol{k} \\ \boldsymbol{b} &= m_{12}\boldsymbol{i} + m_{22}\boldsymbol{j} + m_{32}\boldsymbol{k} \\ \boldsymbol{c} &= m_{13}\boldsymbol{i} + m_{23}\boldsymbol{j} + m_{33}\boldsymbol{k}. \end{aligned} \quad A9$$

For the setting of $\boldsymbol{i}//\boldsymbol{a}$ and $\boldsymbol{k}//\boldsymbol{a}\times\boldsymbol{b}$ (Fig. A2a), the geometrical relations of $\boldsymbol{a}$ and $\boldsymbol{b}$ with respect to the basis vectors of the orthonormal crystal coordinate system are straightforward and can be easily deduced:

$$\begin{aligned} \boldsymbol{a} &= a\boldsymbol{i} + 0\boldsymbol{j} + 0\boldsymbol{k} \\ \boldsymbol{b} &= \mathrm{b}\cos\gamma\,\boldsymbol{i} + \mathrm{b}\sin\gamma\,\boldsymbol{j} + 0\boldsymbol{k} \end{aligned} \quad A10$$

The relations of $\boldsymbol{c}$ with the basis vectors $\boldsymbol{i}$, $\boldsymbol{j}$ and $\boldsymbol{k}$ are less direct and requires exploration. First, we need to resolve the angle between $\boldsymbol{c}$ and $\boldsymbol{k}$, σ, in Fig. A2b that is also the angle between $\boldsymbol{c}$ and $\boldsymbol{n}^*_{\mathbf{001}}$, as $\boldsymbol{n}^*_{\mathbf{001}}$ is the vector normal to the (001) plane, i.e., the $\boldsymbol{a}-\boldsymbol{b}$ plane. This can be done using the scalar product of $\boldsymbol{c}$ and $\boldsymbol{n}^*_{\mathbf{001}}$ (Eq. A6). It should be noted that $\boldsymbol{c}$ is in the direct space and $\boldsymbol{n}^*_{\mathbf{001}}$ is in the reciprocal space, thus, it is convenient to first transform $\boldsymbol{n}^*_{\mathbf{001}}$ to the direct space, using Eq. A3. Then,

$$\boldsymbol{n}_{\mathbf{001}} = \boldsymbol{n}^*_{\mathbf{001}}G^*_{ij}, \quad A11$$

and

$$\sigma = cos^{-1}\left(\frac{n_iG_{ij}c_j}{\sqrt{n_iG_{ij}n_j}\sqrt{c_iG_{ij}c_j}}\right) \quad A12$$

Thus,

$$m_{33} = c\cdot cos\sigma \quad A13$$

To resolve m_{13} and m_{23}, we need two auxiliary vectors, $\boldsymbol{r}$ and $\boldsymbol{t}$, as shown in Fig. A2c. $\boldsymbol{r}$ is orthogonal to $\boldsymbol{c}$ and $\boldsymbol{k}$ or $\boldsymbol{n}^*_{\mathbf{001}}$, and $\boldsymbol{t}$ is the projection of $\boldsymbol{c}$ in the $\boldsymbol{a}-\boldsymbol{b}$ plane with its modulus $t = c\cdot\sin\sigma$. $\boldsymbol{r}$ is also perpendicular to $\boldsymbol{t}$. Obviously, $\boldsymbol{r}$ is parallel to the vector cross product of $\boldsymbol{c}$ and $\boldsymbol{n}^*_{\mathbf{001}}$ and in the $\boldsymbol{a}-\boldsymbol{b}$ plane. According to Eq. A7b, it is convenient to transform $\boldsymbol{c}$ to the reciprocal space and conduct the vectoral product to obtain $\boldsymbol{r}$ in the direct space, as below:

$$\boldsymbol{r} = \boldsymbol{n}^*_{\mathbf{001}}\times(G_{ij}\boldsymbol{c}) \quad A14$$

Thus, the angle between $\boldsymbol{r}$ and $\boldsymbol{a}$, χ, in Fig. A2c, can be calculated using Eq. A6a:

$$\chi = cos^{-1}\left(\frac{a_iG_{ij}r_j}{\sqrt{a_iG_{ij}a_j}\sqrt{r_iG_{ij}r_j}}\right) \quad A15$$

Then, the angle between $\boldsymbol{a}$ and $\boldsymbol{t}$, ε, in Fig. A2c is:

$$\varepsilon = \chi - \frac{\pi}{2} \quad A16$$

With this angle, the coordinates of $\boldsymbol{c}$ on $\boldsymbol{i}$ and $\boldsymbol{j}$ can be resolved as:

$$\begin{aligned} m_{13} &= t\cdot cos\,\varepsilon = t\cdot sin\,\chi \\ m_{23} &= t\cdot\sin\varepsilon = t\cdot\cos\chi \end{aligned} \quad A17$$

Permanent link http://www.atex-software.eu/papers/ATEX_TEM_Aligner_Paper.pdf
D O I https://doi.org/10.1107/S1600576725010118

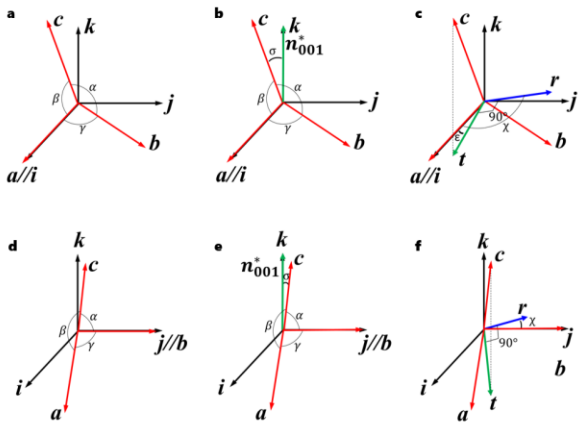

Figure A2. *Geometrical relations between basis vectors of Bravais lattice basis (in black) and those of orthonormal crystal coordinate system (in red). Vectors in green and blue are auxiliary for establish certain specific angular relations between basis vectors of two coordinate systems.*

Following the same deduction logics, the geometrical relations between the basis vectors of the Bravais lattice basis and the orthonormal coordinate system for the setting of $\boldsymbol{j}//\boldsymbol{b}$ and $\boldsymbol{k}//\boldsymbol{a}\times\boldsymbol{b}$ (Fig. A2d) can be obtained as follows:

$$\boldsymbol{a} = \mathrm{a}\sin\gamma\,\boldsymbol{i} + a\cos\gamma\,\boldsymbol{j} + 0\boldsymbol{k}$$
$$\boldsymbol{b} = 0\boldsymbol{i} + b\boldsymbol{j} + 0\boldsymbol{k} \qquad A18$$
$$\boldsymbol{c} = t\cos\chi\,\boldsymbol{i} + t\sin\chi\,\boldsymbol{j} + c\cos\sigma\,\boldsymbol{k}$$

Appendix 3

Fig. A3 illustrates the workflow of the ATEX-software module "TEM-Aligner," which is developed to guide the tilt/rotation operations of the TEM sample holder. As shown in Fig. A3, the interactive user interface for the two-beam condition contains several key components:

1. Selection of the desired diffraction condition (e.g., two-beam or zone-axis on-edge condition);
2. Specification of the crystallographic structure of the sample;
3. Selection of the target reflection (e.g., the (111) reflection used in Fig. A3a);
4. Visualization of the Kikuchi pattern;
5. Input of the crystal orientation in the form of Euler angles;
6. Selection of the sample holder type;
7. Pole figure display of the selected reflection plane(s);
8. Configuration of basic parameters for both the TEM and the sample holder;
9. Output of the required holder tilt angles to achieve the designated diffraction condition;
10. Pole figure plotting and graphical interface for orientation manipulation.

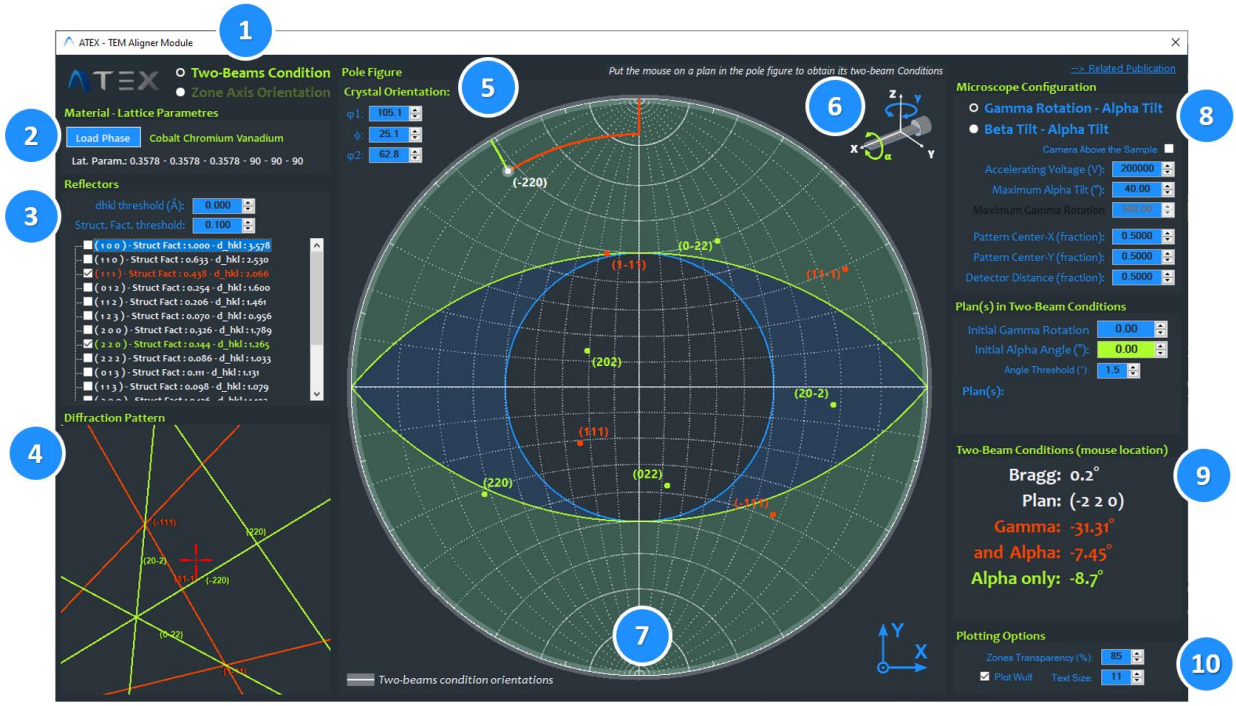

Figure A3. *Developed software module "TEM-Aligner" in ATEX-software for guidance of TEM operation to achieve specific beam conditions.*

Appendix 2

$$M_E = \begin{pmatrix} \cos\varphi_1\cos\varphi_2 - \sin\varphi_1\sin\varphi_2\cos\Phi & -\cos\varphi_1\sin\varphi_2 - \sin\varphi_1\cos\varphi_2\cos\Phi & \sin\varphi_1\sin\Phi \\ \sin\varphi_1\cos\varphi_2 + \cos\varphi_1\sin\varphi_2\cos\Phi & -\sin\varphi_1\sin\varphi_2 + \cos\varphi_1\cos\varphi_2\cos\Phi & -\cos\varphi_1\sin\Phi \\ \sin\varphi_2\sin\Phi & \cos\varphi_2\sin\Phi & \cos\Phi \end{pmatrix} \qquad A19$$

Permanent link http://www.atex-software.eu/papers/ATEX_TEM_Aligner_Paper.pdf
D O I https://doi.org/10.1107/S1600576725010118

Fig. A4(a_1–a_2) and (b_1–b_2) demonstrate how the *TEM-Aligner* module is used to guide the sample holder to reach the $\boldsymbol{g}_{(11\bar{1})}$ and $\boldsymbol{g}_{(2\bar{2}0)}$ two-beam conditions, as previously shown in Fig. 7 for ***Example 1***. Similarly, Fig. A3(c_1–c_2) illustrate the alignment procedure to bring the sample to the [1̄12] zone-axis on-edge condition presented in Fig. 8 for ***Example 2***.

These examples clearly demonstrate that, once the crystallographic orientation of the sample is known, the developed software enables rapid and efficient sample manipulation to achieve the desired diffraction conditions. This significantly reduces the time and effort required for experimental alignment, thereby enhancing the practicality and productivity of advanced TEM operations.

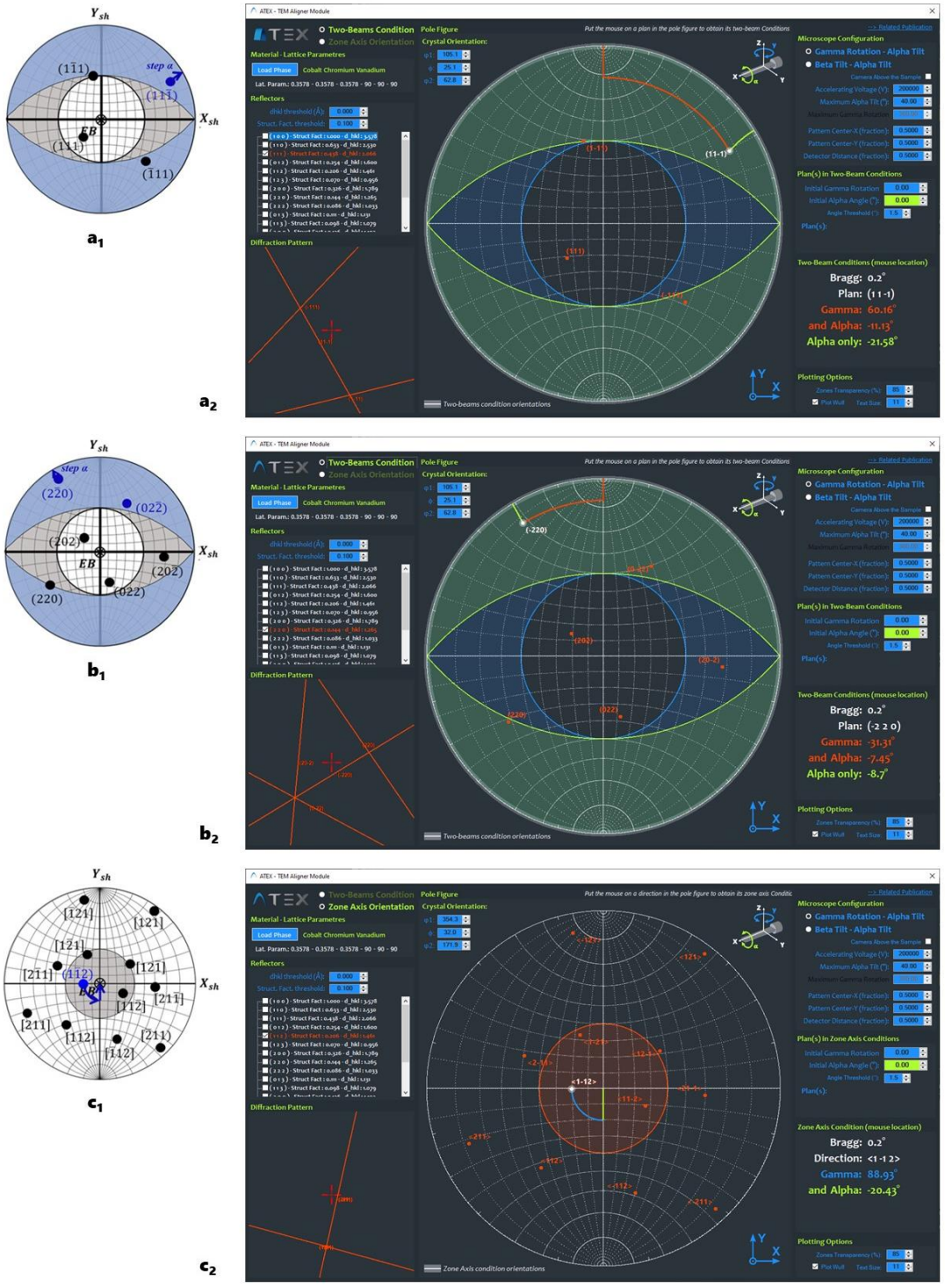

Figure A4. *(a_1-a_2) and (b_1-b_2) To achieve $\boldsymbol{g}_{11\bar{1}}$ and $\boldsymbol{g}_{2\bar{2}0}$ two-beam conditions with respect to Fig. 7. (d_1-d_2) in* **Example 1**. *(c_1-c_2) To achieve [1 1̄ 2] zone-axis on-edge condition with respect to Fig. 8 in* **Example 2**.

Permanent link http://www.atex-software.eu/papers/ATEX_TEM_Aligner_Paper.pdf
D O I https://doi.org/10.1107/S1600576725010118